coatings

MDPI

Article

Influence of Scanning Paths on the Weld Pool Behavior, Microstructure, and Mechanical Property of AA2060 Al-Li Alloy Joints by Laser Beam Oscillation Welding

Yanbo Song [1], Ying Liang [1,*], Hongbing Liu [1], Luchan Lin [2], Yanfeng Gao [3], Hua Zhang [3] and Jin Yang [1,*]

[1] School of Materials Science and Engineering, Shanghai University of Engineering Science, Shanghai 201620, China; songyanbo97@163.com (Y.S.); lhongbing@163.com (H.L.)
[2] School of Materials Science and Engineering, Shanghai Jiao Tong University, Shanghai 200240, China; luchan.lin@sjtu.edu.cn
[3] School of Mechanical and Automotive Engineering, Shanghai University of Engineering Science, Shanghai 201620, China; gaoyf@sues.edu.cn (Y.G.); hzhang@sues.edu.cn (H.Z.)
* Correspondence: liangyinggabi@126.com (Y.L.); jyang@sues.edu.cn (J.Y.)

Abstract: In this paper, the laser beam oscillation welding (LBOW) was utilized to weld a 2 mm thick AA2060 aluminum-lithium (Al-Li) alloy plate. The weld pool behaviors under three scanning paths (pure laser, O-shaped, and ∞-shaped) were investigated. It was observed that the O-shaped scanning path resulted in the most stable welding process. In addition, the weld macroscopic formation, microstructure, and mechanical property between different paths were studied. The results showed that pure laser and ∞-shaped patterns produced welding defects such as spatters and collapse during the welding process, while the O-shaped pattern exhibited good macroscopic formation at varying laser powers. The O-shaped pattern promoted the finest grain in the weld center and reduced the heat input during the welding process. The equiaxed grain zone (EQZ) width of the O-shaped pattern is the smallest compared to the other two patterns at high laser power. In addition to this, the O-shaped pattern could effectively reduce the porosity in the weld. When an O-shaped scanning pattern was adopted at the ideal laser power parameter of 3000 W, the microhardness of the weld center increased by approximately 5.6% compared to pure laser mode.

Keywords: aluminum-lithium alloy; laser beam oscillation welding (LBOW); weld pool behavior; microstructure; mechanical property

check for updates

Citation: Song, Y.; Liang, Y.; Liu, H.; Lin, L.; Gao, Y.; Zhang, H.; Yang, J. Influence of Scanning Paths on the Weld Pool Behavior, Microstructure, and Mechanical Property of AA2060 Al-Li Alloy Joints by Laser Beam Oscillation Welding. *Coatings* **2024**, *14*, 1065. https://doi.org/10.3390/coatings14081065

Academic Editor: Avik Samanta

Received: 25 July 2024
Revised: 18 August 2024
Accepted: 19 August 2024
Published: 20 August 2024

Copyright: © 2024 by the authors. Licensee MDPI, Basel, Switzerland. This article is an open access article distributed under the terms and conditions of the Creative Commons Attribution (CC BY) license (https://creativecommons.org/licenses/by/4.0/).

1. Introduction

Replacing the traditional aeronautical Al alloys with Al-Li alloys is of great value to enhance the comprehensive properties of aerospace equipment [1]. The addition of lithium elements to aluminum alloys results in the formation of Al-Li alloys that retain high-strength, excellent corrosion resistance, and fatigue resistance, while simultaneously reducing specific gravity and enhancing stiffness [2,3]. Consequently, Al-Li alloys hold promising prospects for utilization in contemporary aerospace manufacturing [4,5]. Laser beam welding offers several benefits, including a high energy density, minimal heat input, absence of mechanical contact, and the ability to weld various materials [6,7]. Laser beam welding achieves optimal welds with a high ratio of depth-to-width, a restricted heat-affected zone, minimal deformation, and excellent mechanical qualities due to its significant energy density [8,9]. When the laser beam is welding high-strength aluminum alloys, it will appear to have high reflectivity, spatter, high porosity, and a joint softening phenomenon [10,11]. These problems seriously restrict the application of laser beams in the aluminum alloy welding field. Laser beam oscillation welding (LBOW) is a new type of welding method that uses a galvanometer-type laser head; it can control the beam in a high frequency under different paths, and has many advantages, such as grain refinement, low porosity, and mechanical property strengthening of joints [12,13].

Numerous scholars have conducted studies on the process of laser beam oscillation welding. Thiel [14] demonstrated that the welding efficiency was notably enhanced in laser scanning welding compared to pure laser welding, while the susceptibility of the welding process to focus drift was diminished. The welding process became more efficient as the sensitivity to focal point drift decreased. Ai [15] developed a three-dimensional numerical model to investigate the dynamic behavior characteristics of the weld pool in oscillatory laser welding, and found that the vortices formed in the weld pool-induced complex fluid flow characteristics. Chen [16] employed an ∞-shaped scanning mode for welding 5052 aluminum alloy. The results showed a significant increase in both the depth and width of the ∞-shaped weld compared to a pure laser weld. Similarly, Wang [17] utilized three different scanning paths of the laser beam to weld 5A06 aluminum alloy. The experiments demonstrated that the weld seam under infinitely shaped laser path was effective in reducing the porosity of the weld zone. The cooling rate during the welding process was an important factor affecting the mechanical properties of the material [18,19]; LBOW changed the thermal input of conventional lasers, thus the cooling rate changes. Zhang [20] employed an oscillating laser to join mild steel and observed that the oscillating laser effectively restrained grain enlargement by changing the linear velocity of the laser beam, and enhanced the tensile strength of welded joints. Zhang [21] examined the fundamental mechanism of the O-shaped scanning laser welding process by the application of computational fluid dynamics methodology. The results demonstrated that the O-shaped scanning laser diminished the maximum temperature and temperature gradient while generating a novel vortex within the weld pool, which increased the cooling rate of the weld, thus improving the mechanical properties of the weld seam. In a study conducted by Smith [22], dissimilar metal welding tests were performed using a laser scanning welding procedure with an O-shaped scanning pattern. By accurately manipulating the scanning profile, velocity, and laser intensity, it was possible to effectively manage the heat input in the welded joint, increasing the degree of subcooling and improving mechanical properties. Conversely, it allowed for the regulation of the fusion depth of the joint, effectively suppressing the formation of brittle intermetallic compounds during the welding procedure. Nevertheless, the investigation into the impact of different scanning trajectories on the weld pool shape and joint strength lacks thoroughness. This study investigates the forming mechanism of laser beam oscillation welding in the AA2060 Al-Li alloy using three scanning paths, as follows: pure laser, O-shaped, and ∞-shaped. The research aims to offer fundamental theoretical support for the laser beam oscillation welding process of Al-Li alloy.

2. Experimental Procedures

2.1. Materials

The dimension of the AA2060-T8 Al-Li alloy plate utilized for the experiment was 150 mm × 50 mm × 2 mm, and its chemical composition was presented in Table 1. The heat treatment state was T8, which meant that the solid solution treatment was followed by cold deformation and subsequent artificial aging, and the temperature of it was 155 °C.

Table 1. Chemical composition of AA2060-T8 (wt. %) [23].

Element	Cu	Li	Zn	Mg	Mn	Zr	Ag	Si	Fe	Ti	Al
Percent	3.9	0.8	0.32	0.7	0.29	0.1	0.34	0.02	0.02	<0.1	Bal.

2.2. Equipment and Methods

As depicted in Figure 1, the welding experiment employed a single-module continuous fiber laser (MFSC 5000 W-6000 W) with a maximum power output of 6000 W. The laser welding defocusing amount was 0 mm. The laser beam wavelength was 1064 nm, the pass aperture was 30 mm, the quasi-diameter focal length was 100 mm, and the focused spot diameter was 0.2 mm. Pure argon (99.99%) was employed as the shielding gas

with flow rates of 15 L/min. The High-Speed Camera (KeTianjian, Changsha, China) was utilized to capture photographs with an exposure time of 45 ms, a frame rate of 2200 Hz, and a pulse width time of 45 ms. The diagram illustrating the structure of laser welding is shown in Figure 1. The scanning trajectory is depicted in Figure 2. The beam trajectory was determined by the deflection of the beam deflector, which was controlled by two galvanometer motors operating in orthogonal directions. The beam was swiftly shifted within a specific range to achieve scanning trajectories that were pure laser, O-shaped, and ∞-shaped. The welding parameters are shown in Table 2.

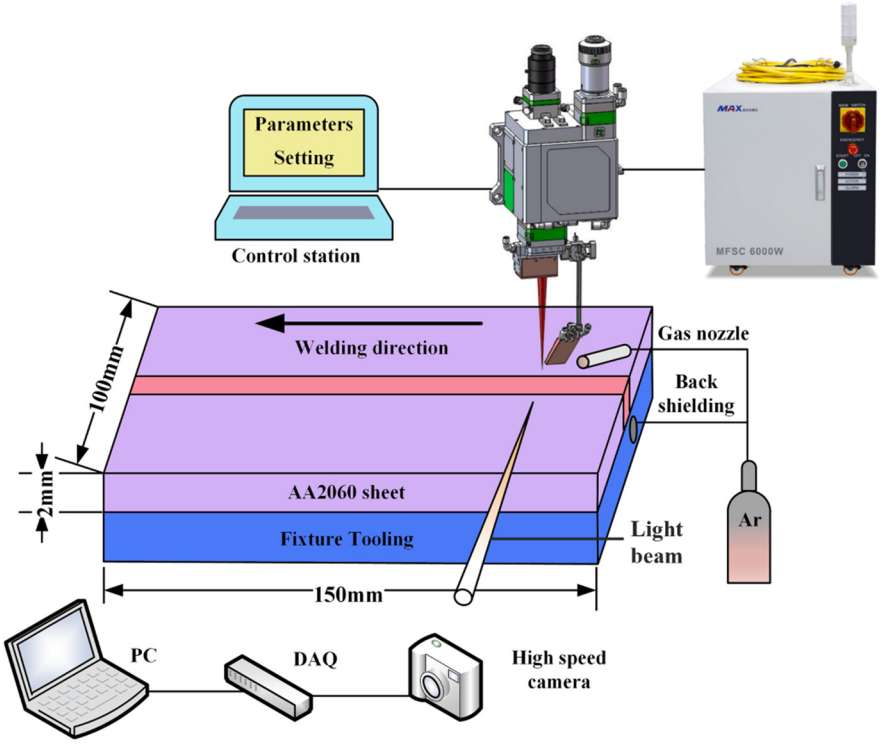


Figure 1. Schematic diagram of the experimental set-up.

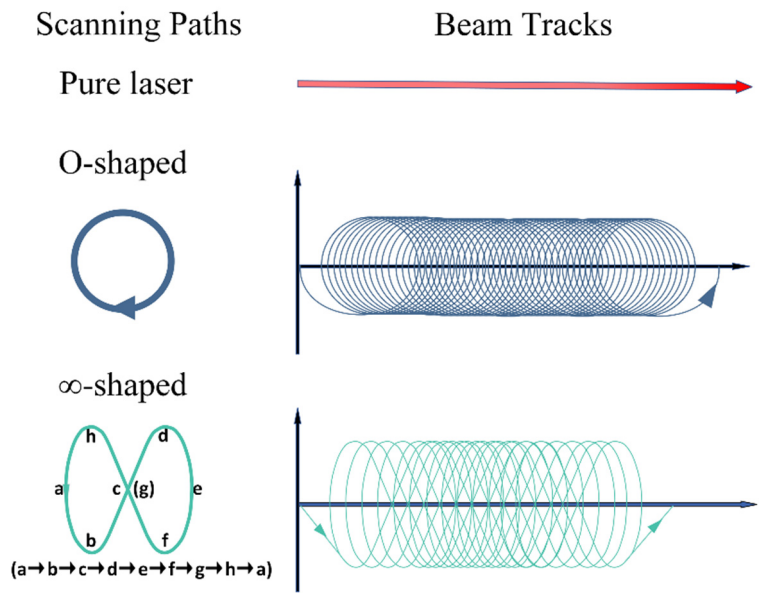


Figure 2. Schematic diagram of the scanning paths and beam tracks.

Table 2. Welding parameters.

Sample	Scanning Path	Laser Power P (W)	Welding Speed V (mm/s)	Scanning Frequency F (Hz)	Scanning Amplitude A (mm)
1	Pure laser	3000	35	0	0
2	O-shaped	3000	35	100	1
3	∞-shaped	3000	35	100	1
4	Pure laser	3500	35	0	0
5	O-shaped	3500	35	100	1
6	∞-shaped	3500	35	100	1

Prior to welding, it was necessary to polish and clean the test plate, and then it was wiped with ethanol to eliminate any surface debris and contaminants. After welding, the metallographic specimen was prepared by making a line cut perpendicular to the welding direction. Subsequently, it was corroded using Keller's reagent (with a volume ratio of H_2O: HF: HCL: HNO_3 = 95:1:1.5:2.5) after embedding, roughing, grinding, and polishing. We utilized the Tescan vega3 scanning electron microscope to observe the microstructure, and employed a Vickers microhardness tester to measure the hardness of the joints. The hardness testing was conducted along the transverse centerline of the joints. As depicted in Figure 3, the hardness sampling points were spaced at intervals of 0.25 mm and 0.5 mm away from the sheet surface. A loading load of 100 g for a sustained loading time of 15 s was applied. As for the microhardness measurement, each microhardness value was the average obtained under the condition of taking three samples for three hardness tests. The confidence interval was 95%, and standard deviation was 1.9% after reviewing the related standards and taking into account experimental errors.

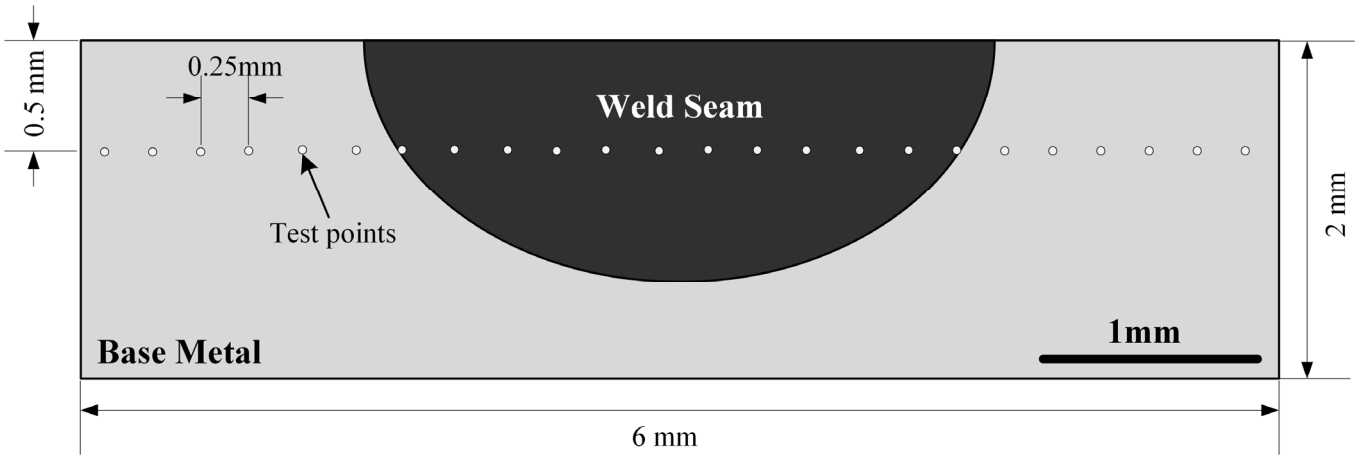


Figure 3. Schematic diagram of the microhardness.

3. Results and Discussion

3.1. Macrostructure

Tables 3 and 4 display the impact of scanning pathways on the surface morphology and cross-section morphology of the weld at different laser power levels. Observations reveal that with a laser power of 3000 W, the surface of the pure laser weld exhibits unevenness, noticeable oxidation, a high concentration of spatters surrounding the weld, and a slight undercut. Upon transitioning to the scanning laser welding technique, there is a notable alteration in the surface configuration of the weld. When the scanning path is O-shaped, the width of the weld path increases significantly, resulting in a uniform silver-white fish scale pattern on the weld surface without oxidation. Additionally, the number of spatters around the weld decreases significantly. On the other hand, when the scanning path is ∞-shaped, the width of the weld path is similar to the O-shaped one. However, the weld surface is less scaly and exhibits better uniformity and smoothness. Nevertheless, when the

laser power is elevated to 3500 W and the scanning path is either pure laser or ∞-shaped, varying levels of undercollapse manifest at the rear end of the weld as a result of heat accumulation, and there is an increased presence of spatter surrounding the weld. At this level of power, the weld production of the O-shaped scanning route remains superior, exhibiting a smooth surface and absence of spatter. Additionally, the breadth of the weld path shows minimal variation at this power level. Hence, it is evident that the utilization of the O-shaped scanning laser welding technique results in improved weld zone formation and enhanced process stability.

Table 3. Surface forming and cross-section morphology of AA2060 weld joints under 3000 W.

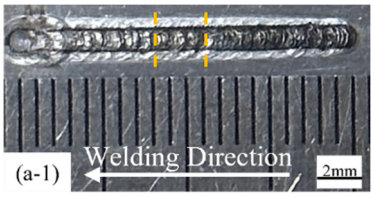
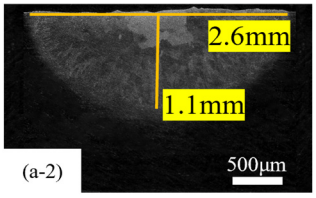
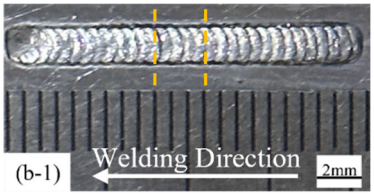
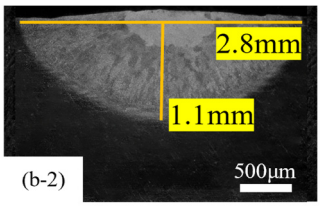
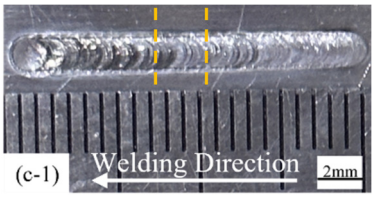
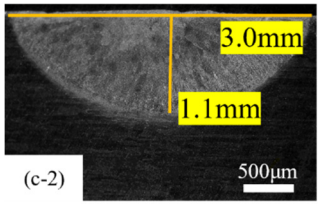
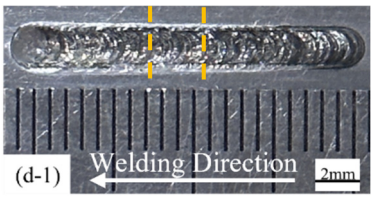
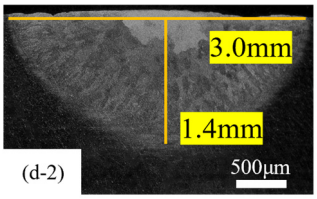
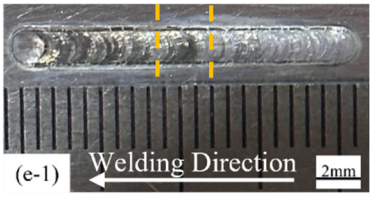
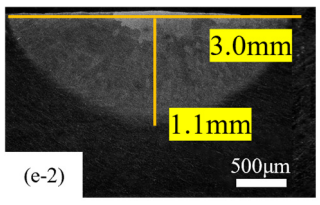
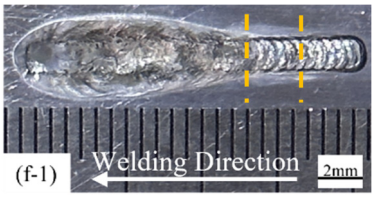
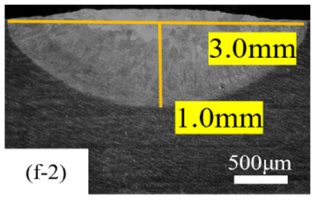
Process Parameters	Top-Surface	Cross-Section
Pure laser		
O-shaped		
∞-shaped		

Table 4. Surface forming and cross-section morphology of AA2060 weld joints under 3500 W.

Process Parameters	Top-Surface	Cross-Section
Pure laser		
O-shaped		
∞-shaped		

As shown in Figure 4, at a laser power of 3000 W, the pure laser produces the smallest weld width in the weld, while the ∞-shaped scanning path produces the largest melt width. This is because the O-shaped and ∞-shaped scanning paths increase the heated area of the weld, leading to an increase in weld width. Additionally, when the scanning paths overlap in a straight line, the weld depth of fusion remains relatively unchanged, regardless of the scanning path. It is evident that the scanning path has a more pronounced impact on the width of the melted area when lower power levels are used. Increasing the laser power to 3500 W results in the greatest weld depth of fusion when using the pure laser. Conversely, the ∞-shaped scanning path yields the smallest weld depth of fusion. However, the weld width remains constant regardless of the scanning path. This is because, at higher power levels, most of the heat is concentrated in the direction of the weld depth of fusion when no swing is applied. On the other hand, the O-shaped and ∞-shaped paths have weaker effects on the depth of fusion than pure laser due to their larger amplitudes, which causes the heat to propagate more rapidly than pure laser.

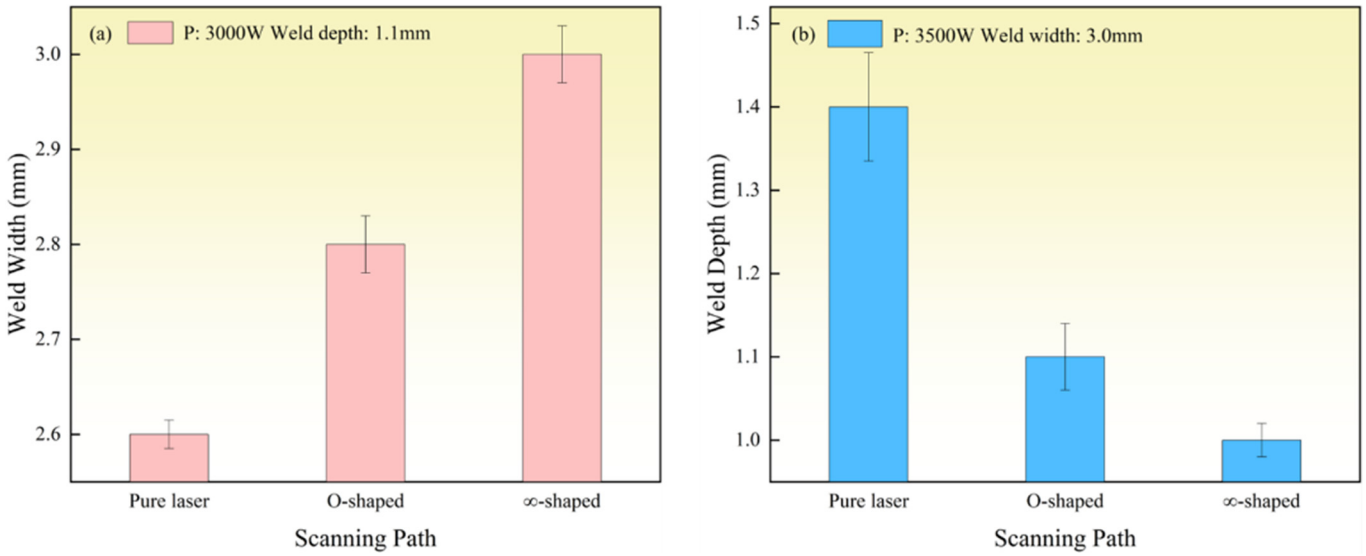


Figure 4. (**a**) Weld width under different scanning paths and (**b**) weld depth under different scanning paths.

3.2. Weld Pool Behavior

High-speed cameras were employed to capture the flow behavior of the weld pool throughout a single cycle under each of the three scanning paths in order to examine the process by which welded connections are formed. The resulting data are presented in Figures 5 and 6.

As depicted in Figure 5a, using a 3000 W laser during the pure laser welding process, a significant portion of laser energy is absorbed by the hole, leading to an elevation in the internal temperature of the hole. Instead, it causes substantial fluctuations in the weld pool and the generation of a substantial amount of plasma and metal vapor. The directional movement of the weld pool is caused by the surface tension gradient of the liquid metal, which is influenced by Marangoni convection. In this scenario, the weld pool oscillation causes some of the molten metal to be expelled when the plasma is emitted from the base metal surface. As a result, spatters are prone to forming on the weld surface.

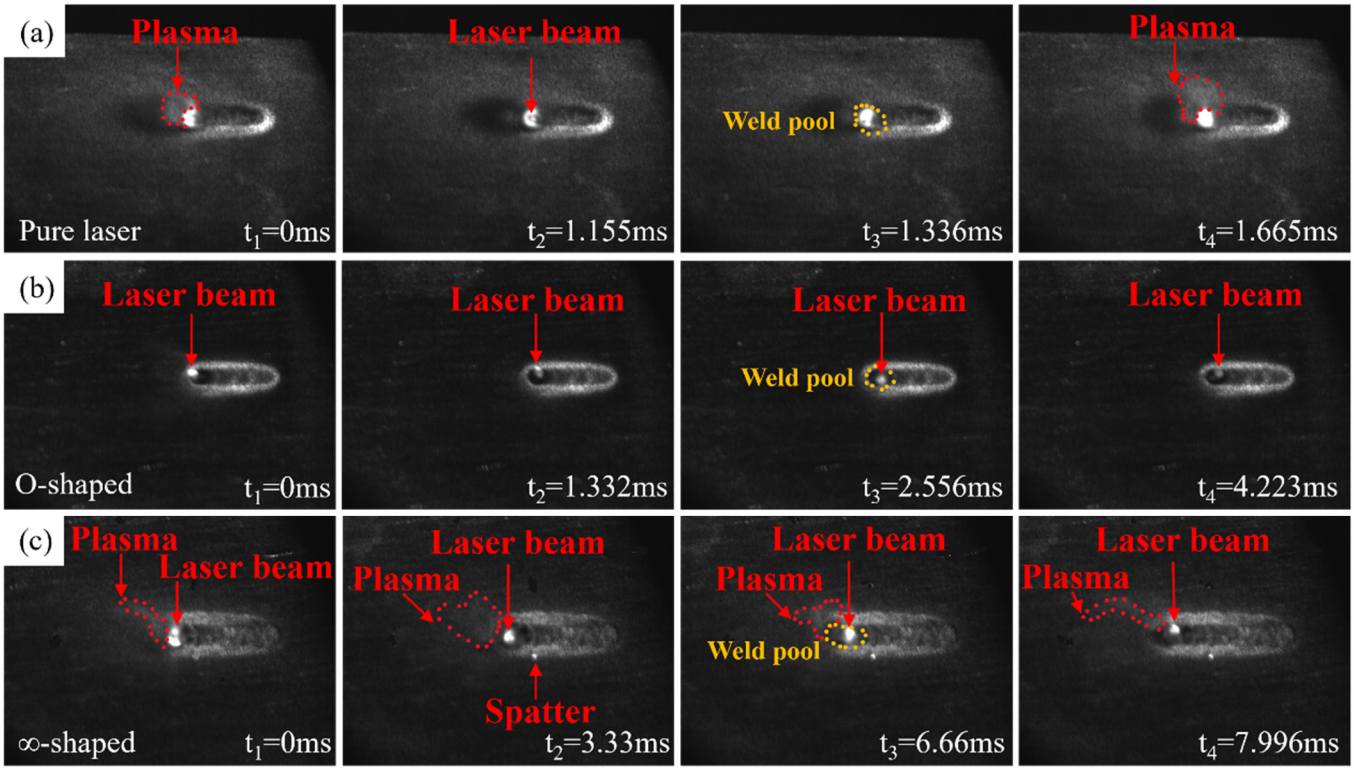


Figure 5. High-speed camera images of 3000 W laser welding: (**a**) pure laser, (**b**) O-shaped, and (**c**) ∞-shaped.

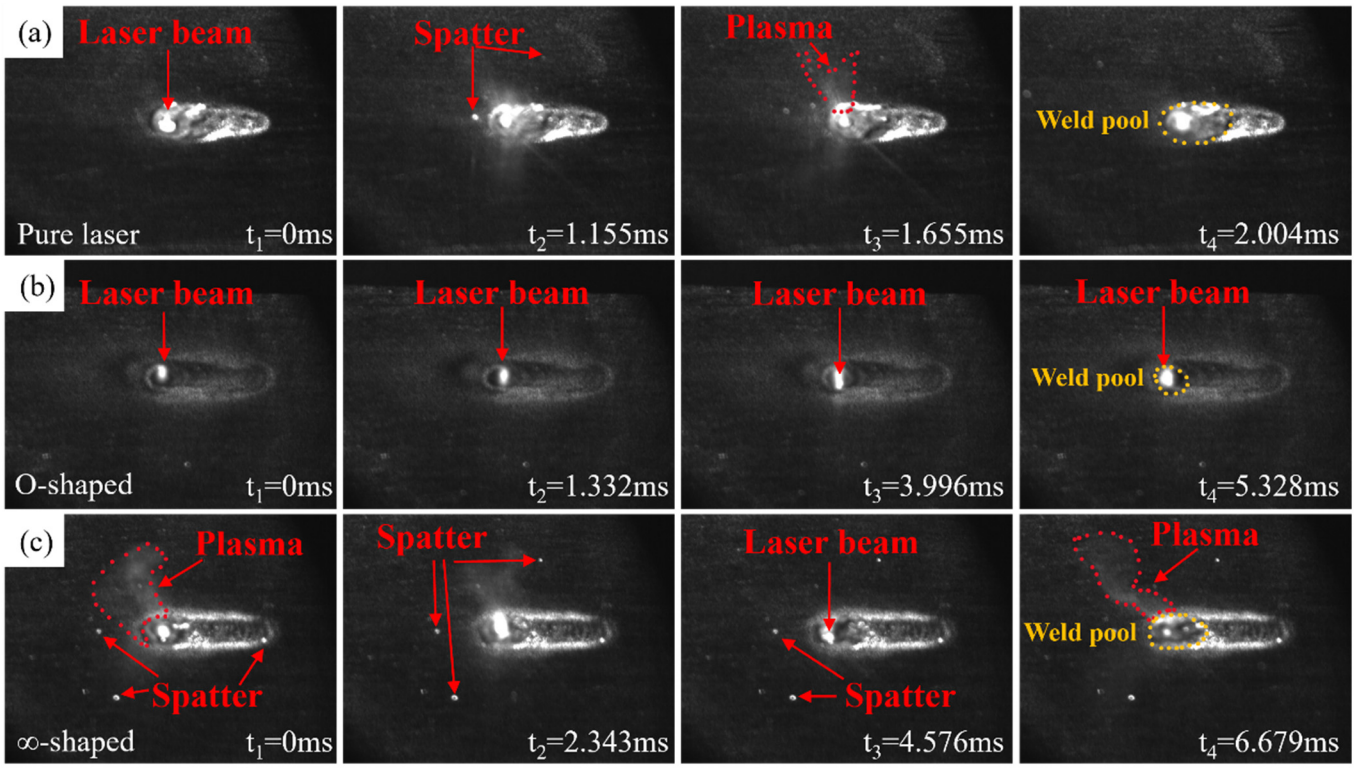


Figure 6. High-speed camera view of 3500 W laser welding: (**a**) pure laser, (**b**) O-shaped, and (**c**) ∞-shaped.

Figure 5b, shows that in the O-shaped scanning welding process, after adopting the O-shaped path, the bursting of plasma/metal vapor is closely related to the change in the laser beam position. As the laser beam position keeps changing, the orientation of plasma also moves, resulting in a decrease in the amount of heat absorbed by the hole. Consequently, this suppresses the bursting of the plasma and the metal vapor. Simultaneously, the velocity of the laser spot's motion is greatly augmented, resulting in the continuous fluctuations in the laser beam position. This dynamic alteration enhances the extent of the impact of the laser beam on the liquid metal, decelerates the rate at which the weld pool cools, reduces the fluctuation of the liquid metal, aids in stabilizing the weld pool, and effectively enhances the uniformity of the weld formation. Furthermore, when compared to the pure laser, the size of the opening in the O-shaped scanning path increases. However, this change in size is relatively gradual and does not exhibit significant fluctuations over time. The high-speed camera shows that the fluctuation of the weld pool surface is relatively smooth, and the splashing phenomenon is significantly reduced.

As can be observed in Figure 5c, in ∞-shaped scanning path laser welding, the volume of plasma and metal vapor is considerably decreased compared to the pure laser welding condition. In this process, the plasma undergoes minimal oscillation while the laser beam follows a distinct "∞" path. The laser beam first melts the alloy at the front end of the weld pool at high temperatures, and then heats the metal at the back end twice as it advances to the back end of the weld pool. The weld pool experiences rapid oscillation, resulting in repeated cycles of cooling, solidification, and heating, leading to a decrease in plasma burst.

As shown in Figure 6a,b, when the laser power is 3500 W, the fluctuation in the size of the weld pool during pure laser and O-shaped scanning welding is comparable to that observed at 3000 W. In Figure 6c, under the ∞-shaped scanning path, the laser power is elevated, resulting in repeated heating of the weld pool and a substantial increase in heat input. The accumulation of heat results in the concentration of heat in the central and posterior regions of the weld, ultimately resulting in the collapse of the liquefied metal pool and the production of substantial quantities of plasma gas and spatter. This phenomenon suggests that when using high power conditions, the thermal treatment of the weld pool during laser welding with a ∞-shaped scanning path becomes unstable. This instability leads to a notable rise in plasma gas and spatter, which has a negative impact on the quality of the weld.

Based on the analysis of the laser scanning weld shaping law, it showed that in the LBOW process, the laser beam constantly changes position. This process can produce two effects. Firstly, it stirs the weld pool, increasing the fluidity of the molten metal to become larger compared to a pure laser case, which allows for stable welding even at lower laser power. Secondly, the continuous movement of the laser beam increases the heating range and the volume of the weld pool that reduces the generation of plasma and metal vapors, resulting in a significant reduction of spatter. An extensive analysis of the outcomes in the two conditions of 3000 W and 3500 W demonstrates that O-shaped scanning laser welding is minimally influenced by the laser power, it exhibits the highest level of stability in the welding process, and achieves an optimal weld shape.

3.3. Microstructure

3.3.1. Crystal Morphology

In order to investigate the characteristic of weld microstructure in the Al-Li alloy during various laser scanning path welding procedures, a scanning electron microscope was utilized to examine the weld structure subsequent to welding. Figure 7 is a schematic diagram of the microstructure of an Al-Li alloy joint, and Figure 8 is the metallographic picture of the actual weld. The weld joint is categorized into four regions based on the heat condition, as follows: the base metal (BM), heat-affected zone (HAZ), transition zone (TZ), and weld zone (WZ). The transition zone consists of the equiaxed grain zone (EQZ) and the partially melted zone (PMZ). The EQZ is a unique fine-grain region between the HAZ and WZ of Al-Li alloy. Several studies have examined the process by which

this region is formed [24–26]. Generally, the weld zone includes columnar dendrites and equiaxed dendrites.

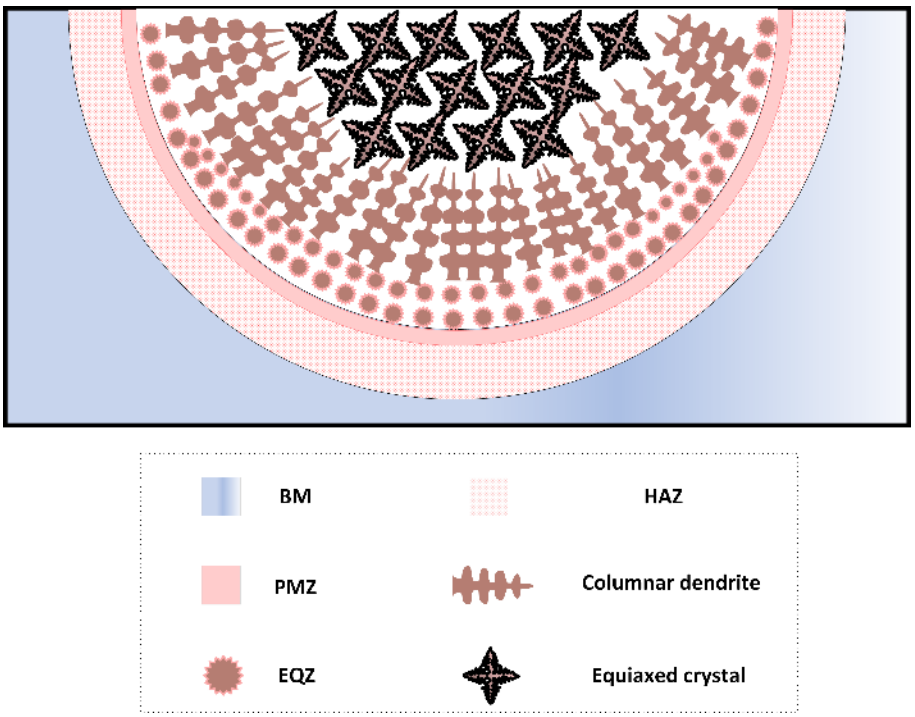


Figure 7. Schematic diagram of microstructure of Al-Li alloy joint.

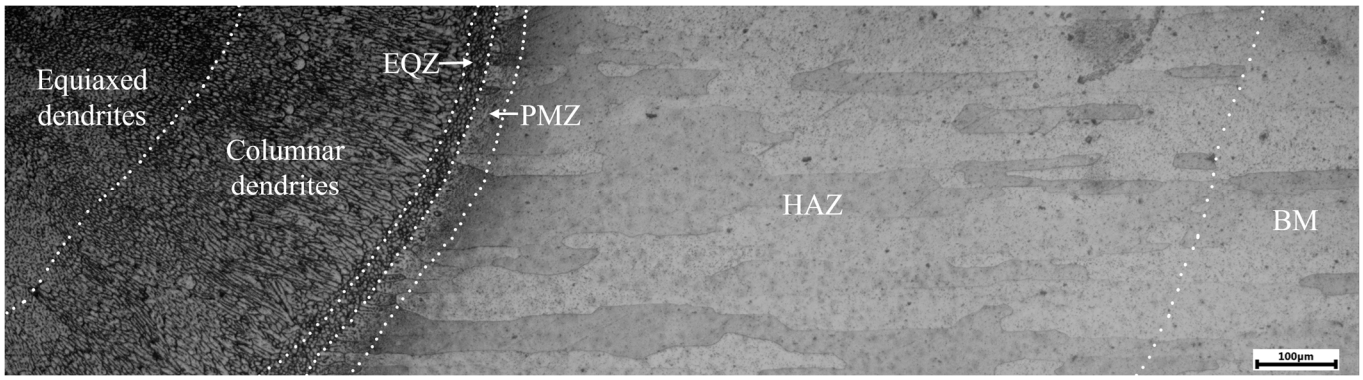


Figure 8. Typical weld metallograph.

During the initial stage of solidification in the weld pool, elevated temperatures and increased welding speeds result in greater temperature differences and faster formation of crystals. In the region of the fusion line near the edge of the weld pool, the temperature is relatively low, making it difficult for the grains to grow, and thus, an EQZ is formed. Figures 9 and 10 show that when the laser power is 3000 W, the EQZ width is 21.76 μm with pure laser, the O-shaped scanning EQZ width is 17.73 μm, and the ∞-shaped scanning EQZ width is 13.69 μm; when the laser power is increased to 3500 W, the EQZ width is 18.71 μm with pure laser, the O-shaped scanning EQZ width is 13.73 μm, and the EQZ width of ∞-shaped scanning is 18.71 μm. Additionally, the width of the columnar dendrites near the fine crystal region also decreases. This phenomenon occurs because the rotational motion of the laser focus alters the temperature gradient of the solid–liquid interface on both sides of the weld pool, specifically in the width direction. As a result, this change affects the process of associative crystallization and ultimately reduces the size of the columnar dendrites. The EQZ zone expands when using ∞-shaped scanning at 3500 W. The reason for this is

that the ∞-shaped scanning applies heat to the weld pool after increasing the laser power. This leads to an excessive amount of heat being applied, and causes fragmentation in the columnar dendrites zone.

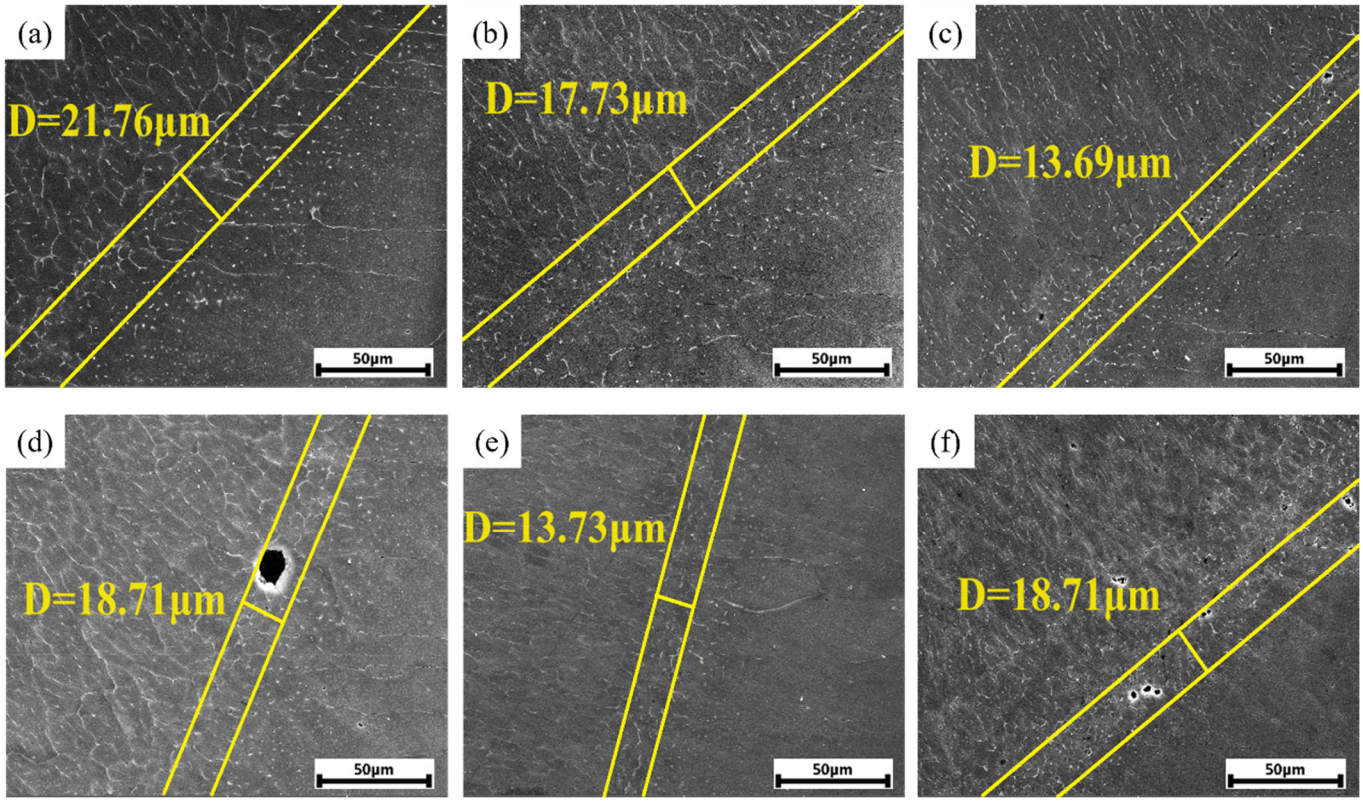


Figure 9. SEM of EQZ: (**a**) 3000 W pure laser, (**b**) 3000 W O-shaped, (**c**) 3000 W ∞-shaped, (**d**) 3500 W pure laser, (**e**) 3500 W O-shaped, and (**f**) 3500 W ∞-shaped.

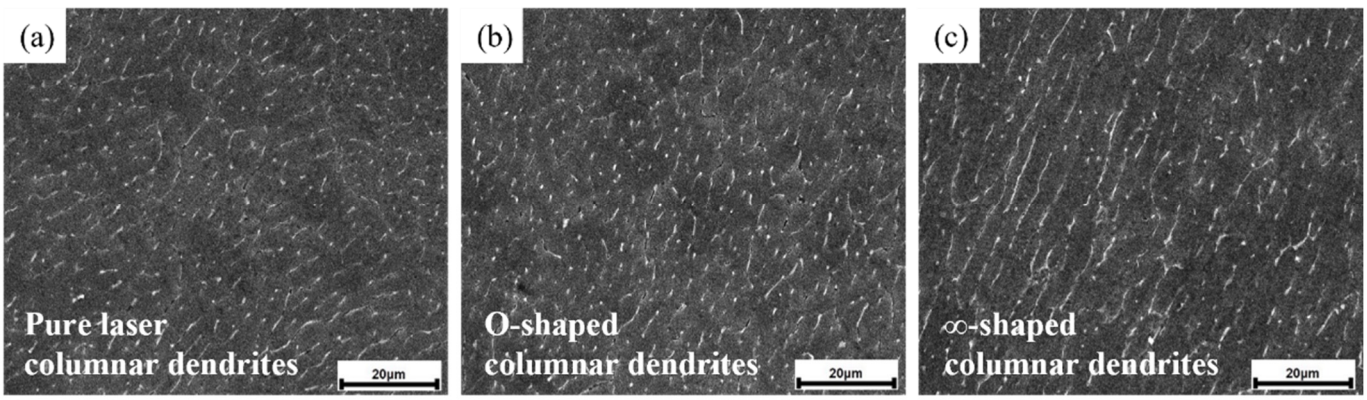


Figure 10. SEM of the columnar dendrites at 3000 W. (**a**) Pure laser, (**b**) O-shaped, and (**c**) ∞-shaped.

When the laser power is 3000 W, pure laser welding and O-shaped laser welding yields a weld with no pores. ∞-shaped laser welding has a small number of pores in the EQZ. When the laser power is 3500 W, pure laser welding yields a weld with larger pores. This is due to the rapid cooling of the weld pool, which prevents the gas from overflowing in a timely manner. The O-shaped laser welding process, due to the laser stirring effect in the weld pool and the stability of the welding process, results in the absence of any obvious pores. In contrast, the ∞-shaped laser welding process, due to the high power welding process instability coupled with a large area of remelting, can easily lead to the inclusion of air in the weld pool, resulting in the formation of pores. The round laser welding, which is

characterized by the laser stirring in the weld pool and the stability of the welding process, does not appear for the formation of any discernible pores. In contrast, the ∞-shaped laser welding, which is associated with the high power welding process and a large area of remelting, is prone to the inclusion of air in the weld pool, which in turn gives rise to the formation of pores.

Figure 10 shows that the high-speed scanning motion of the laser will make the direction of the heat source in the weld continuously change; according to the theory of grain directional growth, the change in the heat source trajectory will inhibit the growth of the columnar dendrites directionality, and will not lead to the emergence of a significant direction of columnar dendrites [27], which can reduce the tendency of the weld cracks.

Figure 11, shows that the grains in the middle of the weld coarsen after adopting the scanning trajectory. Research has demonstrated [28] that the movement of heat and the redistribution of solute elements during the solidification of a weld greatly impact crystal growth. In the case of laser welding of Al-Cu-Li alloys, the initial phase α-Al (gray area) solidifies first. The alloying elements, including Li, Mg, and Cu, become concentrated at the front of the crystalline structure, forming a eutectic arrangement that precipitates around α-Al. The rotational nature of the laser spot leads to localized repeated heating, greater heat input, and extended grain development time, which results in a certain degree of coarsening of the dendritic organization in the center of the weld.

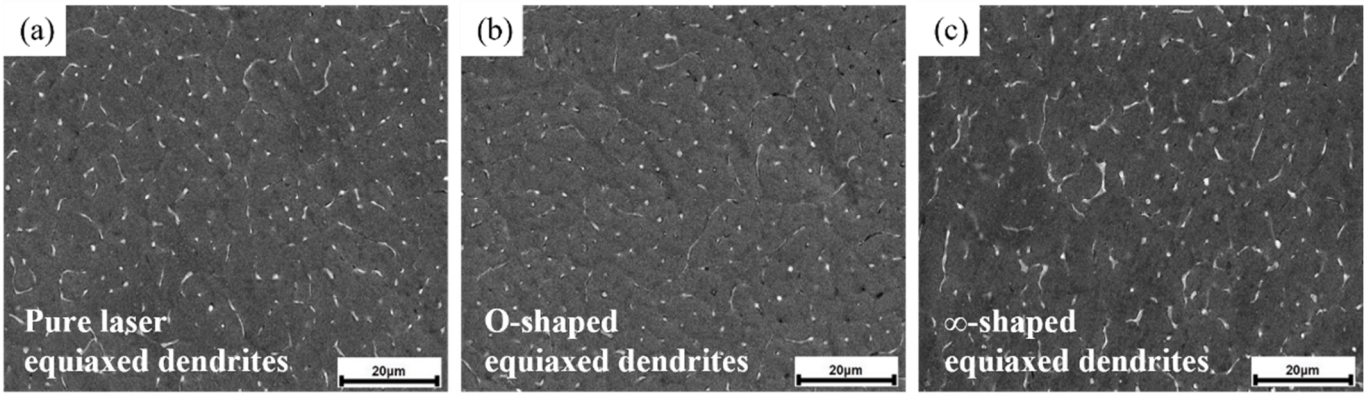


Figure 11. SEM of the equiaxed dendrites at 3000 W. (**a**) Pure laser, (**b**) O-shaped, and (**c**) ∞-shaped.

It can be seen that high-speed welding under the laser scanning welding process does not cause accelerated cooling of the weld pool, and the cooling time of the weld pool can be prolonged relative to pure laser, which helps the crystal nucleation and grain growth; thus, the fine-grain area in the crystallization can be fully nucleated, and can grow into a dense fine-grain area. At the same time, the laser scanning welding process can achieve high-speed changes in the position of the heat source compared to the pure laser welding process, thus inhibiting the directional growth of grains.

3.3.2. Phase Analysis

Li, as a surfactant, comprises approximately 0.8 at. % of the Al-Li alloy. This facilitates the process of being adsorbed onto the surfaces of $A1_3Zr$- and Al_3 (Li, Zr)- precipitated particles [29]. Then, sample 2 was selected for phase analysis. As depicted in Figure 12, EQZ is mainly composed of α-Al (96.64% at. Al) and eutectic Al_2Cu phase (90.05 at. % Al, 8.7% at. Cu). The results of the EDS measurements reveal that the Cu content is less than it is in actuality, due to the fact that the EDS results are coming from an electron/material interaction volume, which is certainly greater in volume than the size of the investigated Al_2Cu phases. In this way the Cu content is certainly lower than the real Cu content of the Al_2Cu phase. As shown in Figure 13, the Zr element has a higher content at grain boundaries than in the α-Al matrix. Based on the theory of molten metal crystallization in welded joints [30], as the weld pool cools and solidifies, solutes are redistributed, resulting

in solute enrichment at the solid–liquid interface side of the weld pool. This enrichment causes compositional supercooling. This process results in the creation of equiaxed nuclei within the areas of the weld pool that have not hardened yet, leading to the growth of equiaxed grains. Furthermore, Zr element promotes grain refinement and equiaxed grain formation through its high tendency to segregate to the liquid/solid interface during solidification [31,32]. For EQZ, the distribution of several solute elements was examined to observe the degree of microscopic segregation of the components. As depicted in Figure 13, the elements Cu, Ag, and Zn have an uneven distribution, with a predominant enrichment at the grain borders and in the spaces between dendrites. This is owing to the non-equilibrium crystallization process that happened in the quick solidification of the weld pool, wherein the higher purity Al crystallizes first, and the crystallization front drives the solute elements from the grain center to the border.

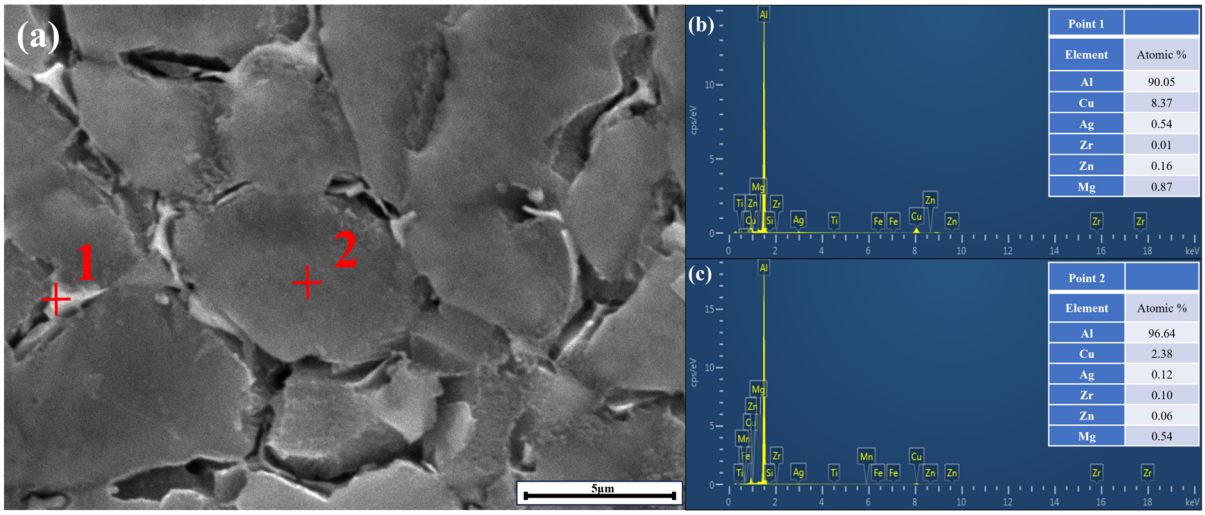


Figure 12. (**a**) The SEM of EQZ (**b**,**c**). The EDS from the zones.

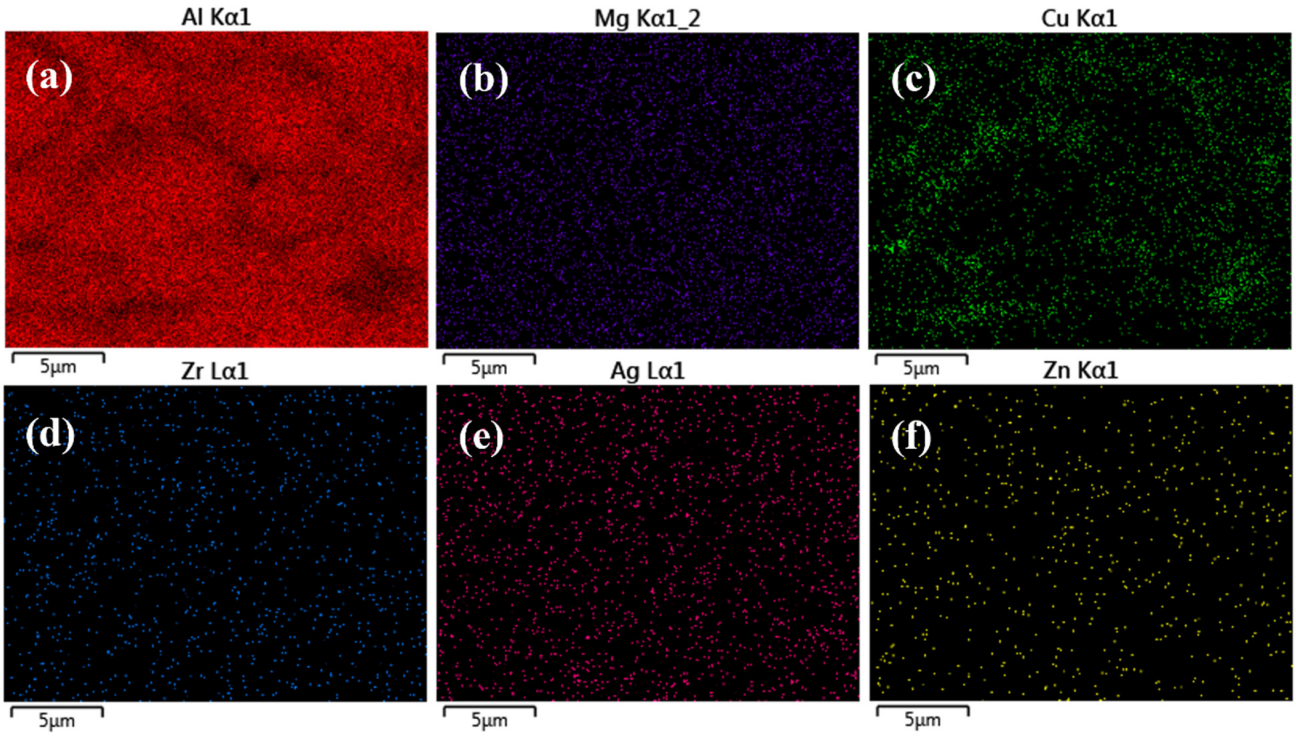


Figure 13. EDS mappings for EQZ. (**a**) Al, (**b**) Mg, (**c**) Cu, (**d**) Zr, (**e**) Ag, and (**f**) Zn.

As made evident in Figure 14, the equiaxed dendrites primarily consist of α-Al solid solution and Al_2Cu eutectic phase, with additional alloying elements being concentrated along the grain boundaries. The EDS analysis reveals that point 3 consists primarily of Al elements (98.21 at. % Al, 0.88 at. % Cu), with lower Cu content compared to the parent material (as shown in Table 1). Points 4 (96.73 at. % Al, 2.41 at. % Cu) and 5 (95.48 at. % Al, 3.45 at. % Cu) exhibit a eutectic structure that is not fully precipitated. As the degree of precipitation increases, the amount of Al decreases, while the content of Cu increases. At point 6, the eutectic phase is fully formed at the borders of the grains, consisting of 92.84 at. % Al and 5.82 at. % Cu. From the Al-Cu binary phase diagram, the maximum solubility of Cu in Al at 548 °C is shown to be 5.65%, whereas the solid solubility of Cu in Al at ambient temperature is 0.05%. The concentration of Cu in the equiaxed dendrites exceeds the maximum amount of Cu that can dissolve in Al. This is due to the rapid solidification and cooling process of the laser weld pool, which expands the solid solubility limit of the alloying elements, and increases the concentration of the alloying elements. As a result, a supersaturated α-Al solid solution is formed in the weld state.

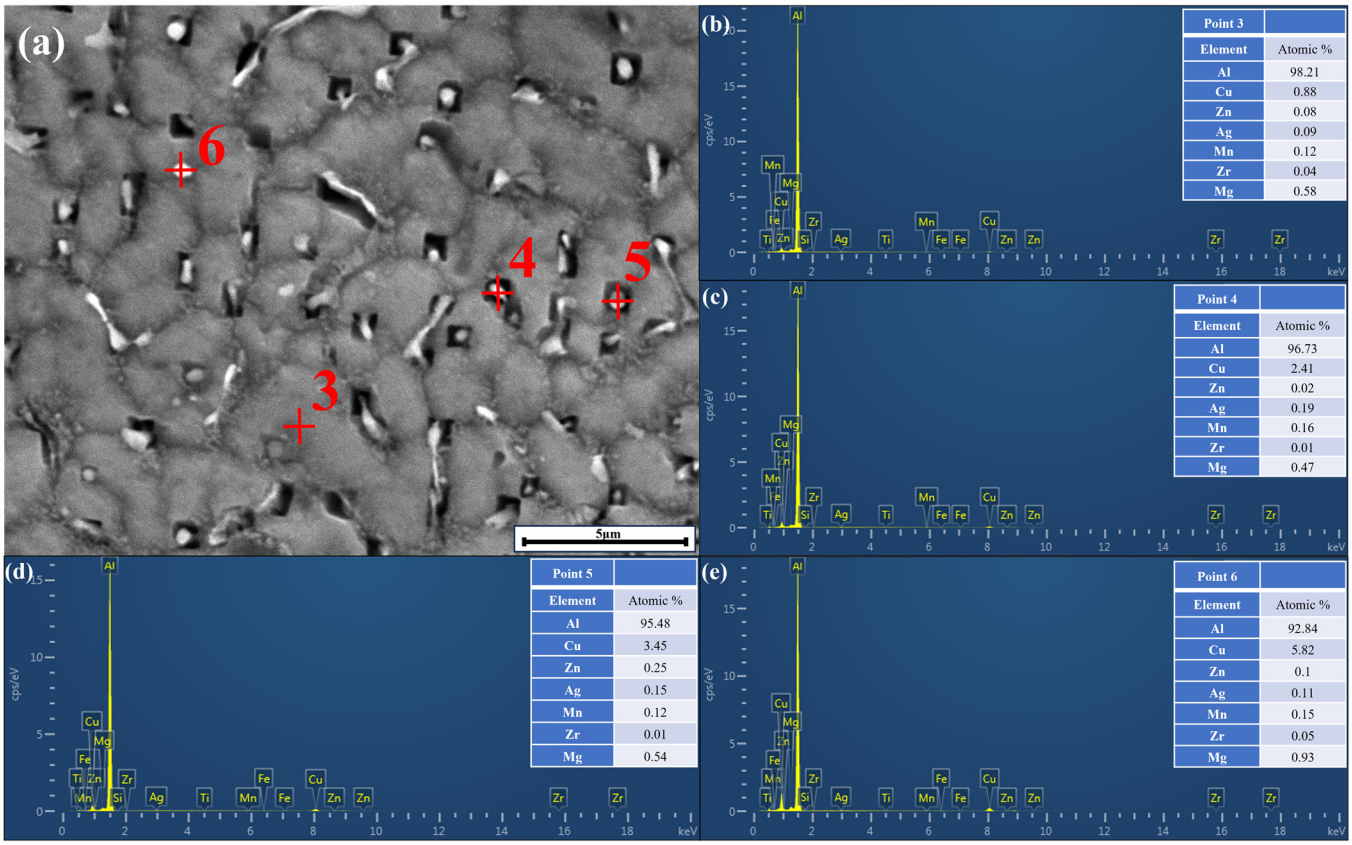


Figure 14. (**a**) The SEM of equiaxed dendrites. (**b**–**e**) The EDS from the zones.

Figure 15 displays the SEM image of the columnar dendrites with EDS spectra, revealing a significant increase in the concentration of Cu elements in the grain boundary precipitates compared to the dendritic center. Conversely, the content of Zr elements is reduced.

As made evident in Figure 16, the grain boundaries and intracrystalline coarse precipitation phases inside the PMZ contain a high concentration of various alloying elements, including both important alloying elements (Cu, Mg, Ag) and ones with a limited diffusion capacity (Fe, Mn). This is because the atomic diffusion coefficients of Fe and Mn are low, preventing them from diffusing into the grain boundaries during the solid-state cooling process of a brief welding heat cycle.

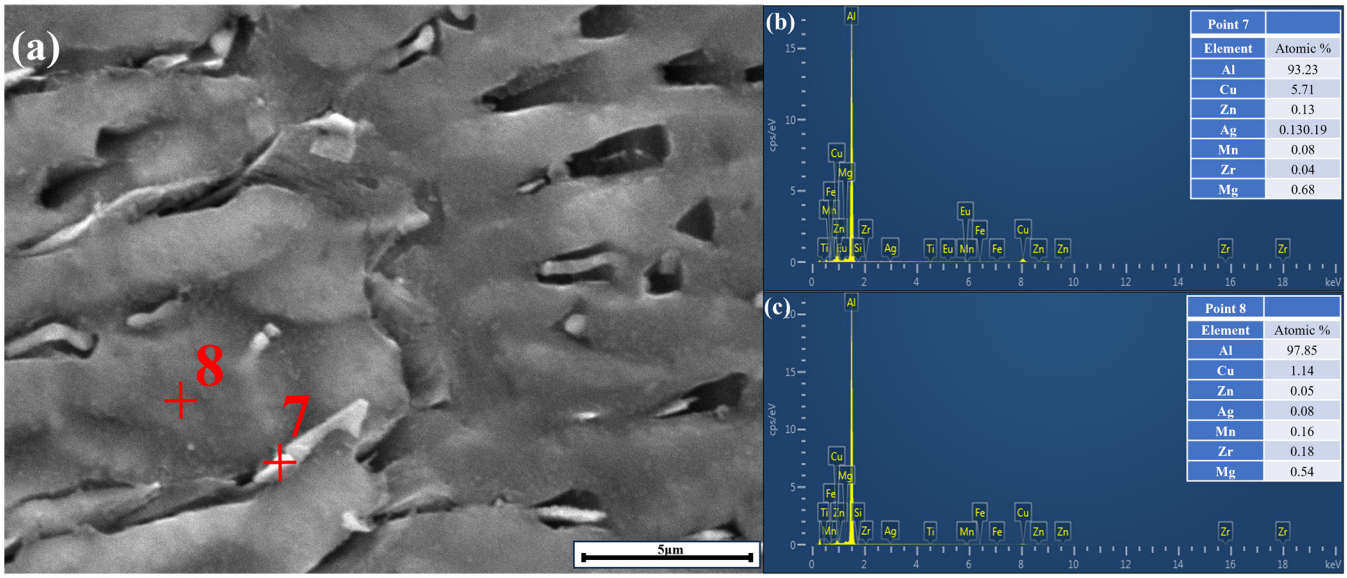


Figure 15. (**a**) The SEM of the columnar dendrites. (**b**,**c**) The EDS from the zones.

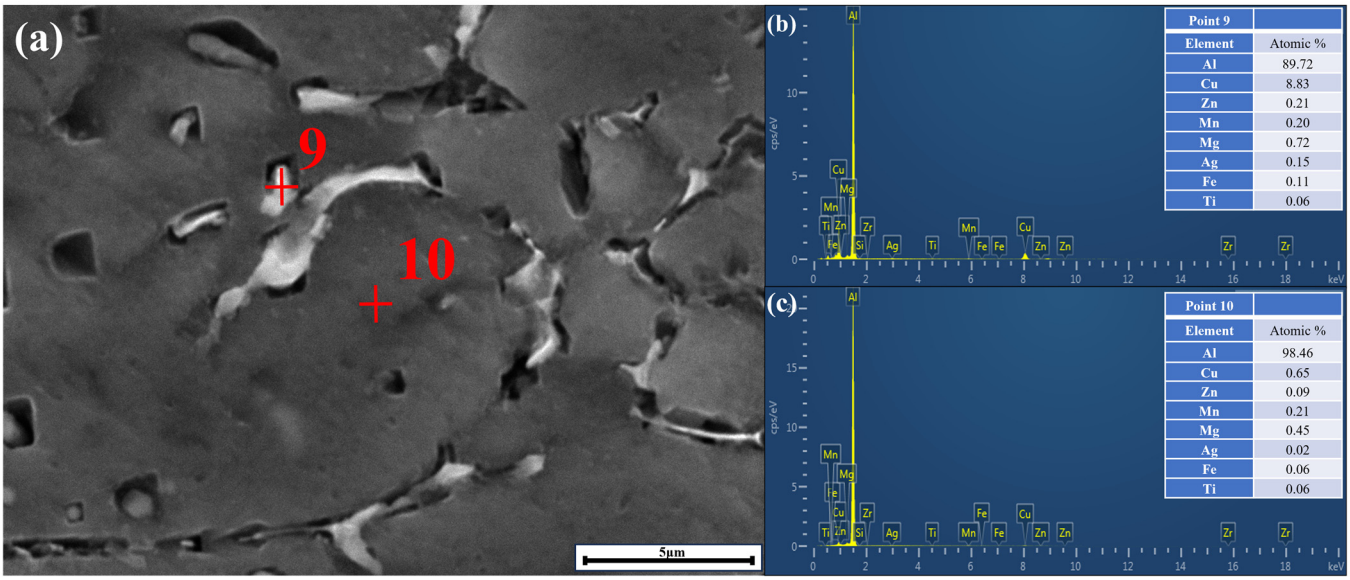


Figure 16. (**a**) The SEM of PMZ. (**b**,**c**) The EDS from the zones.

3.4. Microhardness

A weld joint has equiaxed dendrites, columnar dendrites, EQZ, and PMZ from the center along the direction of the weld fusion line. In Figure 17, it is observed that the microhardness of the weld is low in the equiaxed dendrites. This is due to the fast cooling rate in the center of the weld with low heat input, which may result in the formation of a supersaturated solid solution, leading to low microhardness. As the testing area moves from the equiaxed dendrites to the columnar dendrites area, the microhardness increases. Upon entering the partially melted zone, the microhardness starts to rise rapidly. As the distance between the test point and the center increases, the microhardness quickly returns to the hardness of the base metal.

The comparison reveals that for different powers, low values of microhardness exist in the area of the fusing line for all three. At a power level of 3000 W, the area around the EQZ exhibits a microhardness of approximately 66 HV. However, when the power is increased to 3500 W, the microhardness of the area around the EQZ rises to around 72 HV. During laser welding, the elevated temperature of the base metal adjacent to the fusion line causes

an over-aging phenomenon. This results in the melting of the reinforcing phases inside the base metal, leading to a substantial drop in the microhardness of the HAZ. The scanning path welding procedure does not considerably enhance the softening of the joints in the EQZ. At a power of 3000 W, the equiaxed dendrites microhardness decreases to 40% of the base metal (approximately 65 HV) during the pure laser process. However, when using the O-shaped scanning path process, the hardness of the entire joint becomes more uniform, measuring around 73 HV, which is equivalent to 45.6% of the base metal. Additionally, the microhardness of the joint improves by 5.6% compared to the joint produced through the pure laser process. At a power of 3500 W, the weld microhardness in the equiaxed dendrites is reduced to 41.8% of the base metal microhardness, which is approximately 68 HV, in the pure laser process. In the O-shaped scanning path process, the joint microhardness is more evenly distributed, measuring around 72 HV, which is 44.3% of the base metal hardness. Additionally, the joint microhardness is improved by 2.5% compared to the pure laser process. In the ∞-shaped scanning path process, the joint microhardness is similar to the O-shaped pattern.

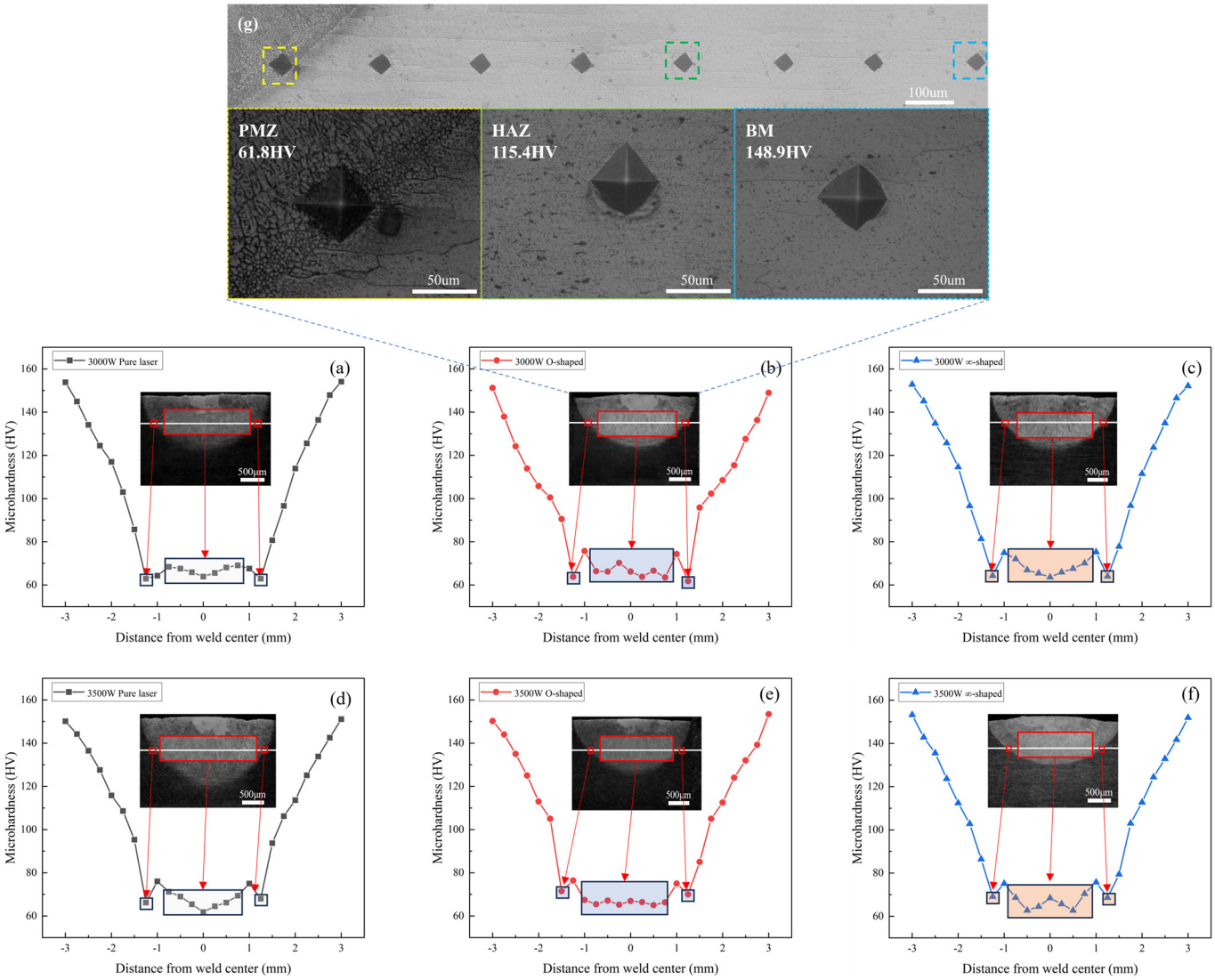


Figure 17. Microhardness distribution of welded joints with different scanning paths. (**a**–**f**) Samples 1–6; (**g**) the track and the value of microhardness in sample 2.

4. Mechanism Analysis

All welding processes used in this experiment are classified as laser heat conduction welding. When using the O-shaped scanning mode, only a small amount of metal evaporated to form vapor depression. As shown in Figure 18, the O-shaped laser beam oscillates in the weld pool, agitating the liquid metal in the weld pool and creating a vortex that reduces the generation of metal vapor and spatters. Additionally, the columnar dendrites in the weld zone are broken up by laser beam, which contributes to the nucleation of fine grains in the center of the weld. Consequently, the O-shaped pattern refines the grain and improves the hardness in the center of the weld when compared to pure laser. At the same time, the O-shaped scanning mode reduces the heat input during the welding process, so the EQZ width of the O-shaped pattern is the smallest compared to the pure laser and ∞-shaped pattern at high laser power. Due to the stirring effect of the laser, the gas can be overflowed in time, so the weld is basically free of pores made by the O-shaped mode.

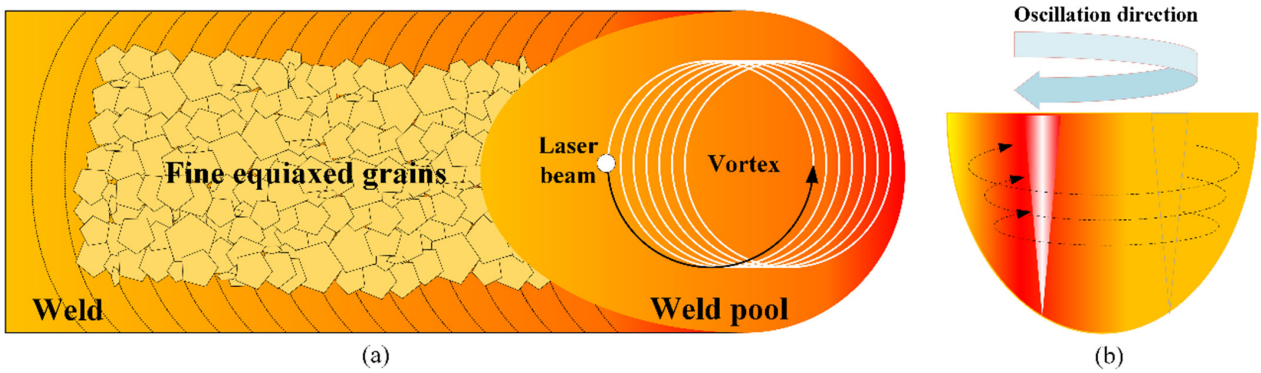


Figure 18. Schematics of weld pool flow and microstructure formation in the O-shaped laser beam welding process: (**a**) top-surface; (**b**) cross-section.

5. Conclusions

In this study, the stability of the welding process, the macroscopic forming, and mechanical properties of the weld under three different scanning paths were studied, obtaining O-shaped mode as the optimal scanning path. The flow state of weld pool and the formation mechanism of grain structure in O-shaped mode were revealed. The main conclusions were as follows:

(1) Laser beam oscillation welding was more effective than pure laser welding in preventing the release of plasma gas and metal vapor from the weld pool, thus reducing spattering. Consequently, the LBOW process was more stable.

(2) The O-shaped scanning path was more resistant to the impact of laser power and yielded the optimal weld shape in comparison to pure laser and ∞-shaped scanning paths.

(3) The Zr element promoted the microstructure formation of EQZ, the equiaxed dendrites and columnar dendrites were mainly composed of α-Al solid solution and Al_2Cu eutectic phase, and PMZ was similar in composition to the base metal.

(4) LBOW could reduce the width of the EQZ and decrease the pores to improve the mechanical properties of the weld, in which the microhardness of the weld center could be increased by 5.6% under a laser power of 3000 W for O-shaped scanning path laser welding compared to pure laser welding, which means that LBOW provides a small improvement in mechanical properties.

Author Contributions: Conceptualization, Y.L., L.L. and J.Y.; methodology, Y.S. and Y.L.; software, Y.G. and H.Z.; validation, Y.L. and Y.S.; formal analysis, Y.S. and H.Z.; resources, J.Y., H.L., H.Z. and Y.G.; data curation, Y.S., Y.L. and Y.G.; writing—original draft preparation, Y.S.; writing—review and editing, Y.L. and J.Y.; project administration, Y.G., H.Z., H.L. and L.L.; supervision, J.Y. and L.L. All authors have read and agreed to the published version of the manuscript.

Funding: This research was funded by the Shanghai Key Laboratory of Materials Laser Processing and Modification (MLPM), grant number MLPM2022-1.

Institutional Review Board Statement: Not applicable.

Data Availability Statement: The data are contained within the article.

Conflicts of Interest: The authors declare no conflicts of interest.

References

1. Li, S.S.; Yue, X.; Li, Q.Y.; Peng, H.L.; Dong, B.X.; Liu, T.S.; Yang, H.Y.; Fan, J.; Shu, S.L.; Qiu, F.; et al. Development and applications of aluminum alloys for aerospace industry. *J. Mater. Res. Technol.* **2023**, *27*, 944–983. [CrossRef]
2. Ma, P.P.; Zhan, L.H.; Liu, C.H.; Wang, Q.; Li, H.; Liu, D.B.; Hu, Z.G. Pre-strain-dependent natural ageing and its effect on subsequent artificial ageing of an Al-Cu-Li alloy. *J. Alloys Compd.* **2019**, *790*, 8–19. [CrossRef]
3. Zhao, Y.Q.; Wu, Y.F.; Chen, M.L.; Gu, Y.Z.; Zhan, X.H. Research on the stripping performance during dual laser-beam bilateral synchronous welding of 2219 aluminum alloy T-joint for spacecraft. *J. Manuf. Process.* **2019**, *45*, 33–45. [CrossRef]
4. Zhang, J.; Wang, C.; Zhang, Y.; Deng, Y.L. Effects of creep aging upon Al-Cu-Li alloy: Strength, toughness and microstructure. *J. Alloys Compd.* **2018**, *764*, 452–459. [CrossRef]
5. Dorin, T.; De Geuser, F.; Lefebvre, W.; Sigli, C.; Deschamps, A. Strengthening mechanisms of T_1 precipitates and their influence on the plasticity of an Al-Cu-Li alloy. *Mat. Sci. Eng. A Struct.* **2014**, *605*, 119–126. [CrossRef]
6. Jiang, N.; Jiang, M.; Chen, X.; Han, T.; Ma, S.; Chen, Y.; Wang, Z.; Jiang, Y.; Yang, L.; Lei, Z.; et al. Effect of beam oscillation on weld formation, microstructure and mechanical properties in vacuum laser beam welding of thick section 5083 aluminum alloy. *Opt. Laser Technol.* **2024**, *171*, 110408. [CrossRef]
7. Zheng, M.; Yang, J.; Xu, J.Y.; Jiang, J.W.; Zhang, H.; Oliveira, J.P.; Lv, X.Q.; Xue, J.; Li, Z.G. Interfacial microstructure and strengthening mechanism of dissimilar laser al/steel joint via a porous high entropy alloy coating. *J. Mater. Res. Technol.* **2023**, *23*, 3997–4011. [CrossRef]
8. Bi, J.; Wu, L.; Liu, Z.; Wang, H.; Li, Q.; Yang, Z. Coupling effect of ultrasonic vibration and beam oscillation on FQZ soften inhibition of laser welded Al-Mg alloy joints. *Mater. Lett. X* **2023**, *18*, 100197. [CrossRef]
9. Jiang, J.W.; Oliveira, J.P.; Yang, J.; Zheng, M.; Li, H.Y.; Xu, W.H.; Wu, L.Q.; Dou, T.Y.; Wang, R.J.; Tan, C.W. Effect of defocusing distance on interfacial reaction and mechanical properties of dissimilar laser Al/steel joints with a porous high entropy alloy coating. *Mater. Charact.* **2024**, *210*, 113751. [CrossRef]
10. Wang, X.; Luo, Y.P.; Huang, T.; Liu, H.X. Experimental Investigation on Laser Impact Welding of Fe-Based Amorphous Alloys to Crystalline Copper. *Materials* **2017**, *10*, 523. [CrossRef]
11. Gong, J.; Li, L.; Meng, S.; Huang, R.; Zou, J.; Cao, H. Study on stability and microstructure properties of oscillating laser welded 5A06 alloy with narrow gap. *Opt. Laser Technol.* **2022**, *155*, 108360. [CrossRef]
12. Liu, F.Y.; Tan, C.W.; Wu, L.J.; Gong, X.T.; Chen, B.; Song, X.G.; Zhao, H.Y.; Wang, G.D. Influence of waveforms on Laser-MIG hybrid welding characteristics of 5052 aluminum alloy assisted by magnetic field. *Opt. Laser Technol.* **2020**, *132*, 106508. [CrossRef]
13. Chen, C.; Wang, W.Y.; Li, D.Y.; Cai, Y.M.; Zhang, Y.H.; Zhang, K. Effect of beam oscillation on microstructure and properties of laser-TIG hybrid welding of D406A ultra-high strength steel. *J. Manuf. Process.* **2020**, *57*, 798–805. [CrossRef]
14. Thiel, C.; Hess, A.; Weber, R.; Graf, T. Stabilization of laser welding processes by means of beam oscillation. *Laser Sources Appl.* **2012**, *8433*, 225–234.
15. Ai, Y.; Yu, L.; Huang, Y.; Liu, X. The investigation of molten pool dynamic behaviors during the "∞" shaped oscillating laser welding of aluminum alloy. *Int. J. Therm. Sci.* **2022**, *173*, 107350. [CrossRef]
16. Chen, G.Y.; Wang, B.; Mao, S.; Zhong, P.X.; He, J. Research on the "∞"-shaped laser scanning welding process for aluminum alloy. *Opt. Laser Technol.* **2019**, *115*, 32–41. [CrossRef]
17. Wang, Z.M.; Oliveira, J.P.; Zeng, Z.; Bu, X.Z.; Peng, B.; Shao, X.Y. Laser beam oscillating welding of 5A06 aluminum alloys: Microstructure, porosity and mechanical properties. *Opt. Laser Technol.* **2019**, *111*, 58–65. [CrossRef]
18. Chmelko, V.; Berta, I.; Margetin, M. Influence of Heat Treatment Process to the Fatigue Properties of High Strength Steel. In Proceedings of the 19th International Colloquium on Mechanical Fatigue of Metals (ICMFM), Porto, Portugal, 5–7 September 2018; pp. 35–40.
19. Wang, Y.; Wu, G.; Zhang, L.; Guo, Y.; Wang, C.; Li, L.; Xiong, X. Microstructure evolution and mechanical properties of a cast and heat-treated Al–Li–Cu–Mg alloy: Effect of cooling rate during casting. *Mater. Sci. Eng. A* **2023**, *880*, 145366. [CrossRef]
20. Zhang, X.D.; Chen, W.Z.; Bao, G.; Zhao, L. Improvement of weld quality using a weaving beam in laser welding. *J. Mater. Sci. Technol.* **2004**, *20*, 633–636.
21. Zhang, C.; Li, X.W.; Gao, M. Effects of circular oscillating beam on heat transfer and melt flow of laser melting pool. *J. Mater. Res. Technol.* **2020**, *9*, 9271–9282. [CrossRef]
22. Smith, S.; Blackburn, J.; Gittos, M.; Bono, P.D.; Hilton, P. Welding of dissimilar metallic materials using a scanned laser beam. In Proceedings of the ICALEO® 2013: 32nd International Congress on Laser Materials Processing, Laser Microprocessing and Nanomanufacturing, Miami, FL, USA, 6–10 October 2013.

23. Xia, L.; Zhan, X.H.; Yu, H.S.; Xia, P.Y.; Feng, X.S.; Wang, Z.D. Morphology and formation mechanism of equiaxed grains along the fusion boundary in Al-Li alloy weld seam. *Mater. Res. Express* **2018**, *5*, 116523. [CrossRef]
24. Cui, G.; Yang, C. Formation and strengthening mechanism of equiaxial cellular grain zone in AA2195-T8 Al–Cu–Li alloy twin-wire P-VPPA welded joint with Ti–Zr microalloying. *Mat. Sci. Eng. A* **2024**, *896*, 146278. [CrossRef]
25. Peng, S.S.; Zou, J.L.; Li, X.T.; Wu, Q.; Xiao, R.S. Fiber Laser High-Frequency Focus Rotation Spot Welding Process Based on Thermal Conductivity. *Chin. J. Lasers-Zhongguo Jiguang* **2018**, *45*, 1102011. [CrossRef]
26. Han, B.; Chen, Y.B.; Tao, W.; Lei, Z.L.; Li, H.; Guo, S.; Li, P. Nano-indentation investigation on the local softening of equiaxed zone in 2060-T8/2099-T83 aluminum-lithium alloys T-joints welded by double-sided laser beam welding. *J. Alloys Compd.* **2018**, *756*, 145–162. [CrossRef]
27. Lei, X.; Nuam, V.L.; Yuan, Y.; Bai, Y.; Yao, W.; Wang, N. Investigation on laser beam remelted Al-Cu-Li alloy part II: Corrosion behavior and mechanical properties. *J. Alloys Compd.* **2021**, *873*, 159765. [CrossRef]
28. Liu, H.B.; Sun, Y.Y.; Xie, R.S.; Chen, Y.; Chen, S.J. Characterization of microstructure and local mechanical properties of friction rolling additive manufactured Al-Li alloy under repeated thermal-mechanical cycles. *Mater. Charact.* **2023**, *204*, 113169. [CrossRef]
29. Jiang, T.; Zhang, M.; Dai, G.; Shen, Z.; Guo, Y.; Sun, Z.; Li, W. Microstructure evolution and mechanical properties of ultrafine-grained Al-Li alloy fabricated via friction stir additive manufacturing. *Mater. Charact.* **2024**, *209*, 113760. [CrossRef]
30. Wang, X.; Liu, W.; Xu, G.; Zhu, J.; Hu, Q.; Du, B. Numerical analysis of dynamic coupling between the keyhole and molten pool in the rotating laser welding process of aluminum alloy. *Int. J. Adv. Manuf. Technol.* **2022**, *121*, 5491–5502. [CrossRef]
31. Hosseini, S.A.; Abdollah-zadeh, A.; Naffakh-Moosavy, H.; Mehri, A. Elimination of hot cracking in the electron beam welding of AA2024-T351 by controlling the welding speed and heat input. *J. Manuf. Process.* **2019**, *46*, 147–158. [CrossRef]
32. Wang, F.; Liu, Z.; Qiu, D.; Taylor, J.A.; Easton, M.A.; Zhang, M.-X. Revisiting the role of peritectics in grain refinement of Al alloys. *Acta Mater.* **2013**, *61*, 360–370. [CrossRef]

Disclaimer/Publisher's Note: The statements, opinions and data contained in all publications are solely those of the individual author(s) and contributor(s) and not of MDPI and/or the editor(s). MDPI and/or the editor(s) disclaim responsibility for any injury to people or property resulting from any ideas, methods, instructions or products referred to in the content.